

CORONAL MASS EJECTION RECONSTRUCTIONS FROM INTERPLANETARY SCINTILLATION DATA USING A KINEMATIC MODEL: A BRIEF REVIEW

M. M. BISI*, B. V. JACKSON, P. P. HICK, A. BUFFINGTON
and J. M. CLOVER

*Center for Astrophysics and Space Sciences
University of California, San Diego
9500 Gilman Drive #0424, La Jolla, CA 92093-0424, USA
*mmbisi@ucsd.edu
mario.bisi@gmail.com

Interplanetary scintillation (IPS) observations of multiple sources provide a view of the solar wind at all heliographic latitudes from around 1 AU down to coronagraph fields of view. These are used to study the evolution of the solar wind and solar transients out into interplanetary space, and also the inner-heliospheric response to co-rotating solar structures and coronal mass ejections (CMEs). With colleagues at the Solar Terrestrial Environment Laboratory (STELab), Nagoya University, Japan, we have developed near-real-time access of STELab IPS data for use in space-weather forecasting. We use a three-dimensional (3D) reconstruction technique that obtains perspective views of solar co-rotating plasma and of outward-flowing solar wind crossing our lines of sight from the Earth to the radio sources. This is accomplished by iteratively fitting a kinematic solar wind model to the IPS observations. This 3D modeling technique permits reconstructions of the density and speed structures of CMEs and other interplanetary transients at a relatively coarse resolution. These reconstructions have a 28-day solar-rotation cadence with 10° latitudinal and longitudinal heliographic resolution for a co-rotational model, and a one-day cadence and 20° latitudinal and longitudinal heliographic resolution for a time-dependent model. These resolutions are restricted by the numbers of lines of sight available for the reconstructions. When Solar Mass Ejection Imager (SMEI) Thomson-scattered brightness measurements are used, lines of sight are much greater in number so that density reconstructions can be better resolved. Higher resolutions are also possible when these analyses are applied to Ootacamund IPS data.

1. Introduction

Interplanetary scintillation (IPS) has been used for solar wind, solar wind transient, and inner-heliospheric observations for over 40 years, e.g.

Refs. 1–7. IPS is the rapid variation in signal received by radio antennas on Earth from a compact radio source, arising from scattering by small-scale (~ 150 km) density inhomogeneities in the solar wind flowing approximately radially outward from the Sun. IPS observations allow the solar wind speed to be inferred over all heliographic latitudes and a wide range of heliocentric distances (dependent upon source strength and observing frequency), e.g. Refs. 1–7. Using the level of scintillation converted to g -level as a proxy, the solar wind density can also be inferred from IPS observations, e.g. Refs. 8 and 9.

As described in detail in Ref. 9, scintillation-level measurements have been available from the Solar Terrestrial Environment Laboratory (STELab)¹⁰ radio antenna at Kiso from 1997 to the present, and more recently from mid-2002 from the STELab radio antenna at Fuji. The New Toyokawa site (see later) will also be used for these measurements. The disturbance factor g is defined by Eq. (1).

$$g = m / \langle m \rangle. \quad (1)$$

$\Delta I/I$ in relation to this equation is the ratio of source intensity variation to measured signal intensity, m is the observed fractional scintillation level, and $\langle m \rangle$ is the modeled mean level of $\Delta I/I$ for the source at the elongation at the time of observation. Scintillation-level measurements from the STELab radio facility analyses are available at a given sky location as an intensity variation of the source signal strength. For each source, data are automatically edited to remove any obvious interference discerned in the daily observations. Further discussion regarding the calculation of and use of g -level as a proxy for density (and also the real-time calculation used for space-weather forecasting) can be found in Refs. 8 and 9.

When two or more radio antennas are used and the separation of the ray-paths in the plane of the sky from source to each telescope lies close to radial (the solar wind flow direction) centered at the Sun, a high degree of correlation between the patterns of scintillation recorded at the two telescopes may be observed, e.g. Ref. 11. The time lag for which maximum cross-correlation occurs (taking into account “plane-of-sky” assumptions) can then be used to estimate the outflow speed of the irregularities producing the scintillation, e.g. Refs. 12 and 13. More sophisticated methods involving the fitting of the observed auto- and cross-correlation spectra with the results from a weak-scattering model, have also

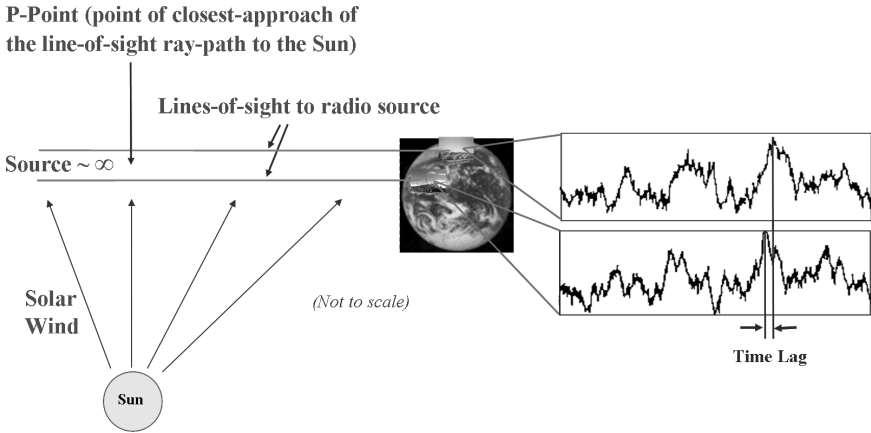


Fig. 1. Figure showing the basic principles of multi-site interplanetary scintillation (IPS) observations through simultaneous observation of a single radio source from multiple (in this case two) antennas. The signal received from a distant, compact source has a variation in amplitude which is directly related to turbulence in the material crossing your line of sight (in this case outflow from the Sun), and thus can be related to variations in density. The example shows similar amplitude variations of signal with a time lag as they pass across the sky from one receiver's line of sight to the other, and are then later used to calculate a measurement of outflow speed. IPS is most sensitive to the point of closest approach to the Sun (P-Point) and to material flowing perpendicular/close-to-perpendicular across the line-of-sight. Figure outline originally courtesy of R.A. Fallows (Aberystwyth University), adapted from Ref. 16.

been adopted for IPS data analyses, e.g. Refs. 7, 14 and 15. Figure 1 shows a picture version of how IPS signals are received using two radio antennas.

The primary sources of data discussed in this chapter were taken from observations made by two different IPS systems. These are the radio arrays of the STELab,¹⁰ University of Nagoya, Japan, and also the Ootacamund (Ooty) Radio Telescope (ORT),^{17–19} India; both systems operate at an observing frequency of 327 MHz and both (the new Toyokawa antenna is shown from STELab) are pictured in Fig. 2. STELab typically observes 20–40+ radio sources per day, and Ooty is currently capable of observing up to 1000 radio sources per day.

We use a purely kinematic solar wind model to yield three-dimensional (3D) speed and density reconstructions⁸ using a technique that obtains perspective views of solar co-rotating plasma²⁰ and of outward-flowing solar wind⁹ crossing our lines of sight from the Earth to the radio sources, by iteratively fitting our model to the IPS data. We then compare the resulting 3D reconstructions with *in situ* measurements from the

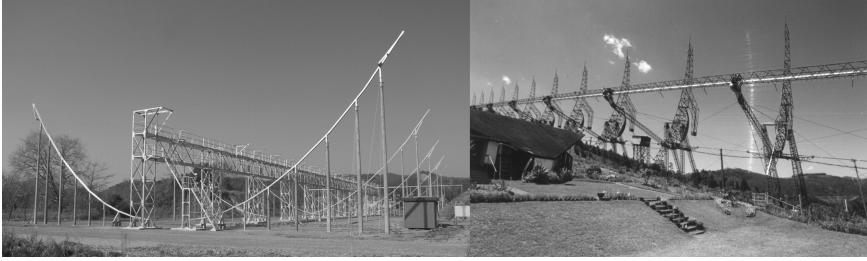


Fig. 2. The new Solar Terrestrial Environment Laboratory (STELab) Toyokawa antenna (left) — currently nearing construction with operation expected in early-mid 2008 (private communication, M. Tokumaru, STELab, 2007), and (right) the Ootacamund (Ooty) Radio Telescope (ORT). (courtesy of <http://www.ncra.tifr.res.in/NSSS-2008/>).

near-Earth Advanced Composition Explorer–Solar Wind Electron, Proton and Alpha Monitor (ACE|SWEPAM),^{21,22} and also with “ram” pressure measurements inferred from the Mars Global Surveyor magnetometer,²³ in an orbit around Mars during the time of this set of observations.

Section 2 summarizes the use of 3D speed and density reconstructions from STELab IPS data when compared with “ram” pressure calculations from the Mars Global Surveyor magnetometer, and preliminary results of a “backsided” set of CMEs with their effects seen at Mars. Section 3 summarizes IPS 3D reconstruction work on a flare-related CME event seen by the Solar and Heliospheric Observatory–Large Angle Spectrometric Coronagraph (SOHO|LASCO)^{24,25} on 2005/05/13. Section 4 summarizes both speed and density reconstructions of some early-November 2004 geomagnetic storms and discusses the density proxy being improved by using the Solar Mass Ejection Imager^{26,27} (SMEI) Thomson-scattered white-light data instead of IPS g -level data for density when compared with ACE *in situ* measurements. Section 5 discusses a preliminary analysis and comparison of 3D density reconstructions from both Ooty and STELab IPS data for the early-November 2004 period, and we will give an overall summary in Sec. 6.

2. 3D Reconstructions: Comparison at Mars

An evaluation of both the co-rotating²⁰ and the time-dependent⁹ models using STELab IPS data at the position of Mars is presented in Ref. 6. Both models are used, the first of the two, the co-rotating model, assumes

that the heliosphere is unchanging except for outward-flowing solar wind over intervals of one solar rotation. This is where solar rotation provides the primary change of perspective view for each observed location. The second of the two, the time-dependent model, allows time to vary with an interval that is short compared with that of a solar rotation; in this case that of a single day. This short interval imposes the restriction that the reconstructions primarily use the outward motion of the solar wind crossing the lines of sight to give perspective views of each point in space. The 3D reconstruction results using STELab IPS data to date are commensurate with (but also limited by) the observational coverage, temporal and spatial resolution, and also the signal-to-noise level of the observations.

The evaluation in Ref. 6 was carried out through the years 1999–2004 (inclusive) and, since there were no direct measurements of solar wind density or velocity at Mars, solar wind ram pressure measurements derived from the Mars Global Surveyor magnetometer data were used as a solar wind proxy. Equation (2), for transforming the IPS reconstructed solar wind speed and density values extracted at Mars, was formulated in Ref. 6.

$$P = mnv^2 = 2 \times 10^{-6}nv^2. \quad (2)$$

Where P is the derived IPS reconstructed ram pressure at Mars, the effective mass per electron (m) is taken to be 2.0×10^{-24} g; P is in nPa, n is electron number density in $\text{e}^- \text{cm}^{-3}$, and v is speed in km s^{-1} .

Jackson *et al.*'s⁶ 3D IPS reconstructions used two different forms of reconstruction at Mars; a summary of their findings can be seen in Fig. 3. The paper identified 47 independent *in situ* “pressure-pulse” events above 3.5 nPa at Mars (the defined threshold for the investigation) in the Mars Global Surveyor data in time periods from 1999 to 2004 where sufficient STELab IPS data were available. 3D reconstructions using both the co-rotating and time-dependent kinematic models were then calculated from STELab IPS data in terms of both speed and density, and from which a value of pressure was calculated to compare with the Mars *in situ* data using Eq. (2). Time-series of pressure were then plotted from each data set and peaks above 3.5 nPa in the Mars Global Surveyor *in situ* data were compared and cross-correlated in time with corresponding peaks from the reconstructed 3D IPS models.

Even though no “perfect” match was found between the two differing IPS reconstruction models and the inferred *in situ* ram pressure measurements, a very good correlation in time for peak amplitudes was found between each of the models and the recorded data at Mars. Successful

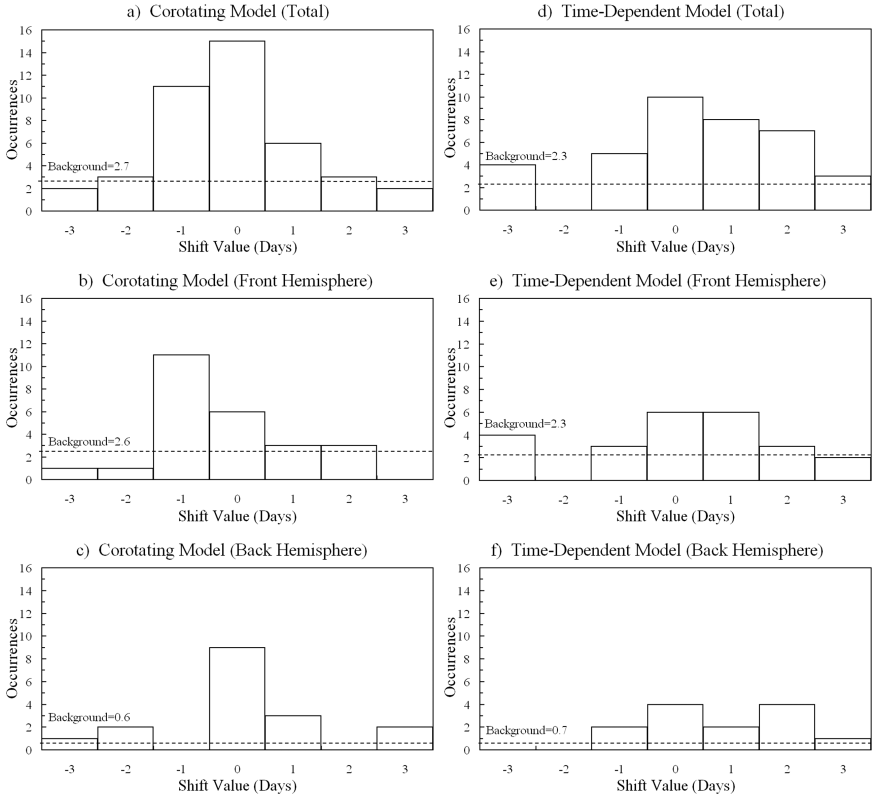


Fig. 3. Mars IPS reconstruction event summary from Ref. 6. The histograms show the time lags/leads between peaks in “ram” pressure that were inferred from the Mars Global Surveyor *in situ* measurements with the corresponding peaks reconstructed in 3D by both the co-rotating and time-dependent models from the STELab IPS observations. A positive time shift indicates a lag in the 3D model relative to the Mars *in situ* proxy and a negative shift indicates a lead in the 3D model relative to the Mars *in situ* proxy. Part (a) shows the total number of corresponding events; (b) the “front-sided” corresponding events; and (c) the “back-sided” corresponding events for the co-rotating model reconstructions. Part (d) shows the total number of corresponding events; (e) the “front-sided” corresponding events; and (f) the “back-sided” corresponding events for the time-dependent model reconstructions.

correlation persisted even when Mars was on the opposite hemisphere of the Sun from the Earth.

An interesting observation from Ref. 6 that was based on the assumption that associations of peaks from the Mars *in situ* analyses and peaks in the IPS modeling analyses are accurate (within a few days), then

the IPS modeling yields solar-wind ram pressures slightly decreased, by about 15%, relative to the pressures observed *in situ* at Mars. This means that the IPS modeling processes produce a lower solar wind speed, a lower solar wind bulk density, or possibly a combination of the two. Moreover, since the Mars Global Surveyor proxy does not account for all terms in the pressure balance, this slightly lower limit on the solar-wind ram pressure indicates that these unaccounted terms must be rather minor contributions to the total Mars magnetospheric solar-wind pressure.⁶

In addition, based on the study carried out by Ref. 6, a peak that appeared just below the 3.5 nPa ram pressure threshold at Mars is thought to be associated with a series of CME events seen in the period 2004/05/30 (30 May 2004) to 2004/06/07 by the SOHO|LASCO instrument which included a back-side Halo CME and several West-limb CME events — these effects were observed at Mars both in the *in situ* data and with the time-dependent IPS reconstruction as seen in Fig. 4. The events are only a “glancing-blow” to Mars, which is likely the cause of the 2–3 day time differential between the two plots at around 9 June 2004, with the reconstruction lagging the arrival time seen *in situ*. This event was first discussed by Refs. 28 and 29.

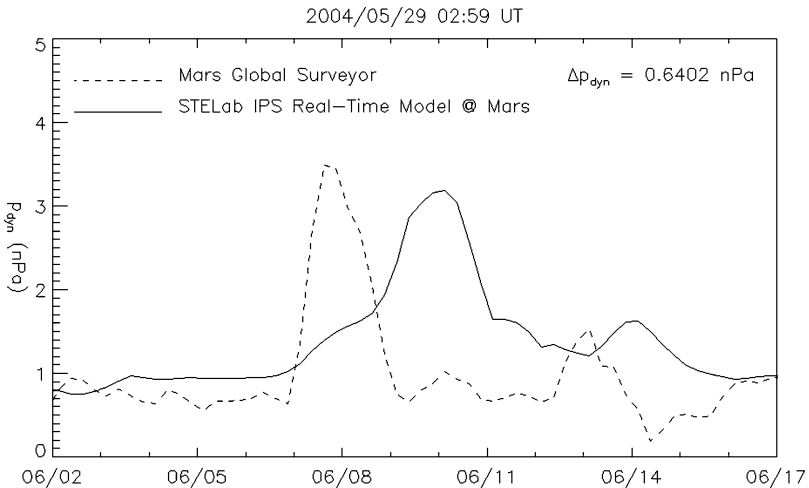


Fig. 4. A time-series of solar-wind ram pressure (nPa) from June 2004 as inferred at Mars from the Mars Global Surveyor magnetometer data (dashed) and also as extracted at the position of Mars from the 3D reconstructed STELab IPS data using the time-dependent model (solid). This is a preliminary analysis adapted from Refs. 28 and 29.

3. 13 May 2005 Flare-Associated CME

The first IPS paper to discuss the 2005/05/13 event was Ref. 30 and this Halo CME has been subsequently discussed by Refs. 31 and 32. A radio-burst resulted from the flare and dimming regions. Both the flare and dimming regions can be seen in the SOHO — Extreme ultra-violet Imaging Telescope (EIT),³³ and circled in Fig. 5. The LASCO images of the CME launch can be seen in Fig. 6.

An interplanetary CME/Magnetic Cloud (ICME/MC) signature was seen by ACE on 2005/05/15. A summary plot from the ACE spacecraft of the solar-wind pressure, magnetic field, radial velocity, and proton density during this day can be seen in Fig. 7. Further details can be found in the captions to the figures.

Again, using g -level as a proxy for density from the STELab IPS observations, we reconstruct the STELab IPS data using the technique described in Ref. 9 and used in Refs. 6, 31, 32 and 34. Note the approximate shape and structure of the ICME as it approaches the Earth on 2005/05/14 as shown in Fig. 8. This is a similar structure to the East of the Sun–Earth line as that seen by SOHO|LASCO in Fig. 6. The timing of the arrival of the event at the Earth from the density reconstructions is approximately consistent with the timing measured by ACE.²⁸

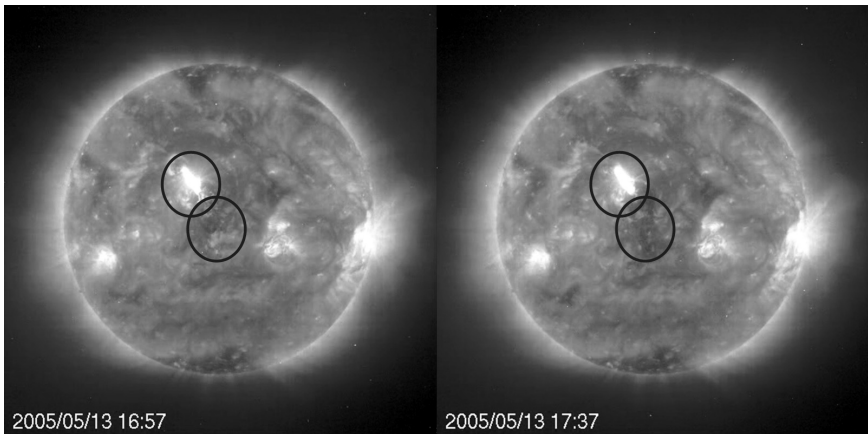


Fig. 5. 2005/05/13 SOHO|EIT images (courtesy of the EIT Consortium) at 16:57 UT (left) and 17:37 UT (right). The active region responsible for this flare/CME (bright area circled) along with associated dimming region (dark area circled) are easily seen. This was a relatively long-lasting active region.

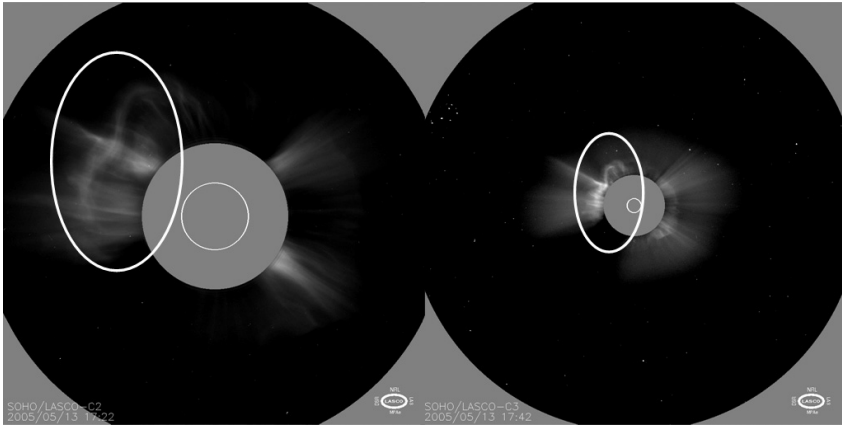


Fig. 6. SOHO/LASCO images of the 2005/05/13 CME, taken from Ref. 32 (courtesy of the LASCO Consortium). The Halo CME pictured at 17:22 UT in LASCO C2 (left) and at 17:42 UT in LASCO C3 (right) with an estimated LASCO speed of 1689 km s^{-1} . CME first C2 appearance was on 2005/05/13 at 17:12:05 UT and the CME first onset at $1R_{\odot}$ was on 2005/05/13 at 16:47:34 UT. Notice the double loop-like structure (circled) to the East of the Sun–Earth line in both images.

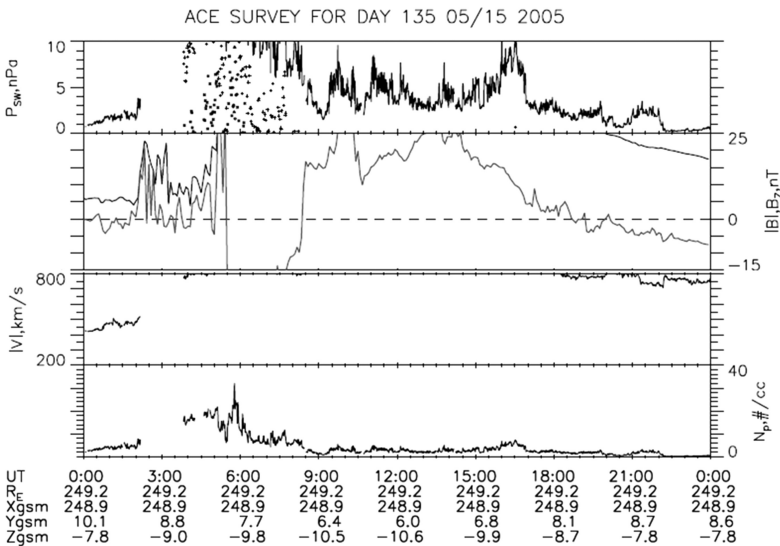


Fig. 7. The ACE solar wind and magnetic field summary data for 2005/05/15, Day of Year (DOY) 135 (adapted from http://pwg.gsfc.nasa.gov/cgi-bin/gif_walk). ACE detected an ICME/MC peak radial velocity on 2005/05/15 of around 1000 km s^{-1} . From the top down: the solar wind pressure in nPa; the absolute magnetic field value (black) and B_z (gray) in nT; the absolute velocity value in km s^{-1} (mostly off the scale); and the proton density in number of protons per cubic centimeter.

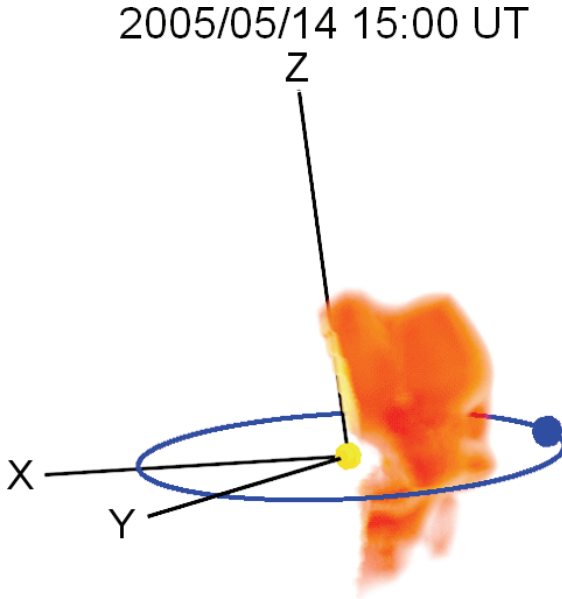


Fig. 8. 3D tomographic reconstruction of the distribution of solar wind density at 15:00 UT on 2005/05/14 as derived from the STELab IPS g -level data using the method described in Ref. 9. All non-associated features of the 2005/05/13 CME (such as behind the Sun relative to the Earth, or in the foreground/background) have been removed. The Sun is represented by the central sphere and the Earth by the outer sphere with its orbital path marked by an ellipse. The view is that of a remote observer East of the Sun–Earth line at a distance of approximately 1.5 AU. The X and Y axes define the Earth’s orbital plane and the Z axis is perpendicular to this into the northern heliospheric hemisphere. The lighter the shade, the greater the density in the reconstruction. Density is shown from $8 \text{ e}^- \text{ cm}^{-3}$ upward with the square decrease with distance from the Sun removed. Note the double loop-like structure weakly seen here East of the Sun–Earth line which is similar to that seen by LASCO in Fig. 6 but expanded out to over 0.5 AU.

The IPS observations from the radio telescopes of the Multi-Element Radio Linked Interferometer Network (MERLIN)³⁵ and the European Incoherent SCATter Radar (EISCAT)^{36,37} when used to perform extremely long-baseline (ELB) IPS observations, can provide a higher resolution for detecting multiple streams crossing the line of sight and also to the direction of flow, e.g. Ref. 38, of the solar wind across the line of sight, e.g. Refs. 12, 39 and 40. As the baseline for an IPS observation increases, so does the ability to detect and resolve multiple solar wind streams crossing your line of sight at a compromise of reducing the overall level of the signal cross-correlation between the simultaneous IPS signals from two different telescopes of the same radio source.¹⁵ The term ELB IPS has been used since Ref. 39 to

describe IPS observations with baselines around 1250 km or greater, e.g. Ref. 12.

A large meridional flow was detected in one of the streams in the EISCAT–MERLIN ELB observations which was first thought to be associated with the 2005/05/13 CME.⁴⁰ The 3D density reconstruction was used to constrain the ELB ray-paths by projecting the line of sight from the Earth to the IPS radio source through the 3D volume, and estimating break-points in the form of an angle relative to the Sun to place different structure in different places along the line of sight. From this method of constraining the ELB ray-paths, Breen *et al.*³¹ found that there were most likely three different streams detected in the observations which corresponded to three peaks from their weak-scattering tri-modal model⁷ used to fit the ELB IPS observations. Previously, Bisi⁴⁰ had reported that the large off-radial flow detected was possibly due to the flow of the ICME/MC itself, but by using the tri-modal fit constrained more accurately by the 3D density reconstruction, it was found that the large meridional flow ($\sim 7^\circ$ – 10° pole-ward) is more likely that of the deflected fast solar wind to the solar North of the ICME/MC,^{31,32} and not a meridional flow of the ICME/MC itself. The ICME/MC detected by the ELB IPS observations was most likely flowing in a radial direction, although this is not fully determined. It is not clear whether the large pole-ward meridional flow is the direction of the flow of material, or is attributed to a deflection of the magnetic-field North of the ICME/MC. In addition, this 3D tomography was also applied using the time-dependent model for the first time to combined MERLIN/EISCAT/EISCAT Svalbard Radar⁴¹ (ESR) IPS data in Ref. 32.

4. Early-November 2004 Geoeffective CME-Events

This early-November 2004 period was a time of complex activity where multiple CME features (including several Halo CMEs) were seen in both the coronagraph images and their interplanetary counterparts from spacecraft *in situ* plasma and magnetic-field measurements near the Earth. This period included several ICMEs that occurred due to a series of solar eruptions originating from the Sun between 2004/11/04 and 2004/11/08. During this period, there were two ICMEs/MCs which had their magnetic orientations in the opposite direction to one another despite the fact that these events were related to flares coming from above the same active region on the Sun, where that active region's magnetic configuration remained unchanged

throughout.⁴² A thorough description and discussion of the *in situ* response to these two major geomagnetic storms can be found in Ref. 42.

The Living With a Star (LWS) Coordinated Data-Analysis by Refs. 43 and 44 also includes these early-November 2004 events during their extensive analyses of large geoeffective storms. They defined their large storms as having a Dst (disturbance storm time index) ≤ -100 nT for storms occurring between the years 1996 and 2005. They list two possible sources for each of the two large storms defined by the Dst criterion with the first storm being on 2004/11/08 and the second on 2004/11/10. The sources for the first storm were seen in SOHO|LASCO C2 on 2004/11/04 at 23:30 UT and at 09:54 UT. The second storm's sources occurred on 2004/11/07 at 16:54 UT and 2004/11/06 at 02:06 UT. Both Refs. 43, 44 and Ref. 42 report that there were multiple interplanetary scintillation signatures caused by each of these two geomagnetic storms.

Also part of the LWS Coordinated Data-Analysis work was carried out by Ref. 34. They show a combination of 3D reconstructions using data from SMEI in terms of Thomson-Scattered white-light brightness as a proxy for density (preliminary analyses), and STELab IPS observations in both g -level (as a proxy for density) and speed. They compared reconstructed structures of SMEI density and STELab IPS speed for events during the early-November 2004 period with *in situ* measurements taken by the ACE spacecraft in order to help validate the 3D tomographic reconstruction results. The geomagnetic storms were fairly well reproduced in both the preliminary SMEI density and the IPS speed reconstructions in terms of their timing with LASCO events and with *in situ* comparisons. Figure 9, taken from Ref. 42, shows the STELab IPS density and speed reconstructions on 2004/11/09 at 03:00 UT. This shows the Earth-directed structure seen in 3D as viewed by a remote-observer at around 1.5 AU.

Initial IPS-only 3D reconstructions for these events were good for the speed when compared with ACE measurements, but were not so good for density.²⁹ IPS speed incorporated into the SMEI reconstructions yielded a better shape for the *in situ* ACE comparisons, and also resulted in a slightly higher correlation of the results as seen in Fig. 10.

The SMEI reconstructions are at a higher temporal and spatial resolution, typically ~ 3 times finer in resolution than those of the IPS reconstructions. SMEI reconstructions are currently limited only by computer analysis considerations and the resulting computation times. This is due to the much more numerous available lines of sight since SMEI is not restricted by the number of bright astronomical radio sources in the sky

2004/11/09 03:00

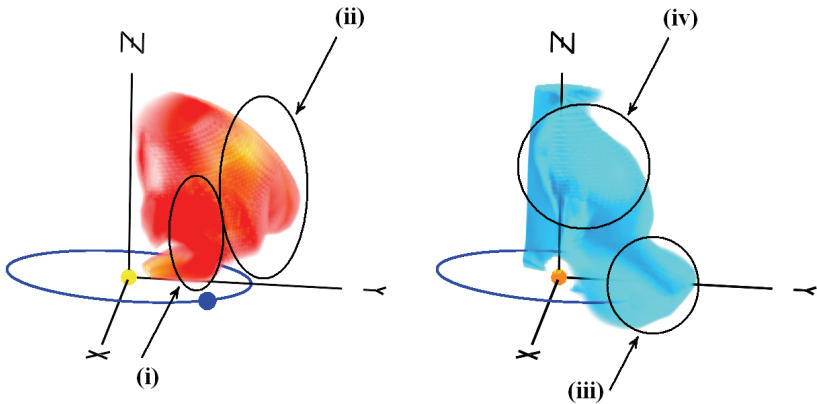


Fig. 9. 3D STELab IPS density (left) and speed (right) tomographic reconstructions, taken from Ref. 42. The reconstructions show the distribution of solar wind density and speed on 2004/11/09 at 03:00 UT. The reconstructions were again carried out using the method described in Ref. 9. All non-associated features have been removed. In both cases, the Sun is represented by the central sphere and the Earth by the outer sphere with its orbital path marked by an ellipse. The view is that of a remote observer partially East of the Sun–Earth line out to a distance of approximately 1.5 AU. The X and Y axes define the Earth’s orbital plane and the Z axis is perpendicular to this into the northern heliospheric hemisphere. The lighter the shade, the greater the values of each parameter in the reconstructions. Density is shown from $15 \text{ e}^- \text{ cm}^{-3}$ upward to $50 \text{ e}^- \text{ cm}^{-3}$, with the square decrease with distance from the Sun removed, and speed is shown from 900 km s^{-1} and up. Various points are marked on the figure and are summarized from Ref. 42. (i) Shows the 2004/11/07 event as seen in LASCO C2 at 16:54 UT. (ii) Shows the combination of the two 2004/11/06 events as seen in LASCO C2 at 01:31 UT and 02:06 UT. (iii) Shows a high speed structure engulfing the Earth; this structure which lags the 2004/11/06 events but precedes the 2004/11/07 event is also comparable in speed to that detected by LASCO C2 for the 2004/11/07 event. Finally, (iv) shows high speed solar wind going mainly northward; consistent with the speeds of (iii).

(as is the IPS). To compare with ACE proton density measurements, the present preliminary analysis includes an electron excess due to helium and heavier ions and conversion from SMEI surface-brightness units (analogue-to-digital units, ADUs) to S10 of $0.5 \text{ ADU} = \text{one S10}$ was used by the tomography here. An S10 is the intensity of a 10th magnitude star filling one square-degree of sky (see Ref. 45). IPS speed data were incorporated along with the SMEI brightness data (as described by Ref. 46) to improve the global propagation times of SMEI density structures coming out from the Sun in the SMEI reconstructions. The SMEI reconstructions here have bins of 6.7° by 6.7° in latitude and longitude at a 1/2-day temporal cadence. This is described in detail in Ref. 46. The comparison in Fig. 10 shows the

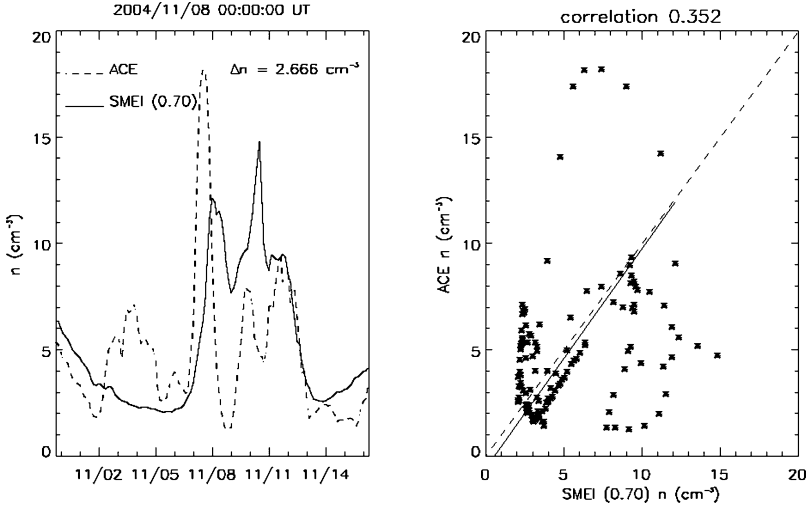


Fig. 10. Comparison plot of SMEI reconstructed density incorporating the IPS speed proxy extracted at the point of the ACE spacecraft for direct-comparison with *in situ* measurements — November 2004 events adapted from Ref. 29. The left plot shows the comparison of the reconstructed density values extracted at the position of the ACE spacecraft from the SMEI Thomson-scattered white-light brightness observations (solid line) and those measured by ACE (dashed line). On the right is a plot of the correlation of these two data sets, the dotted line where a 100% correlation would be found having a one-to-one correspondence. The solid line represents the best-fit of the correlation between the two data sets. Further details are covered in Ref. 34.

ACE data averaged with box-car averaging over a 1/2-day cadence to match that of the SMEI temporal cadence.

The shapes in the reconstructions reproduced around the Earth from the SMEI data show the combination of the several Earth-directed events. These are consistent with the timings of the geoeffective storms described in Ref. 42. The IPS speed data show the fast CME speeds seen in LASCO heading to the North and North-West as well as engulfing the Earth in some high speed wind consistent with what was seen *in situ* at ACE.

5. Preliminary Ooty–STELab 3D Density Reconstruction-Comparisons

Some preliminary analyses using the 3D kinematic time-dependent model have been carried out on the early-November 2004 period with Ooty IPS g -level data comparing with STELab g -level data in terms of density

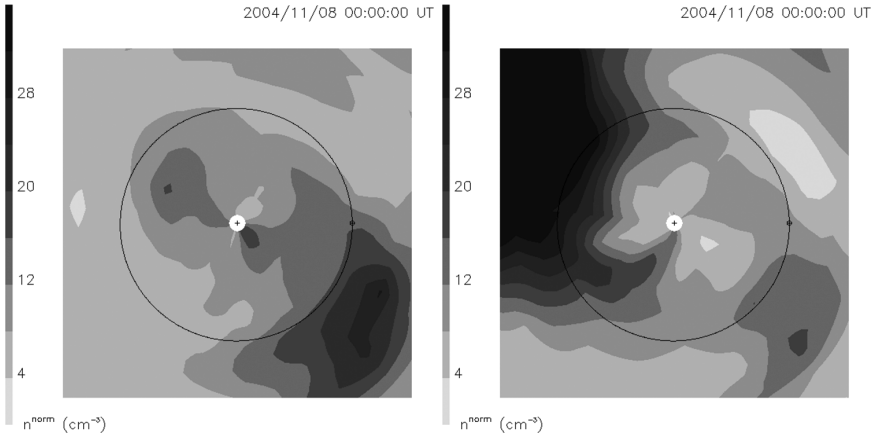


Fig. 11. Figure showing a side-by-side comparison cut in the ecliptic-plane as if looking down from the North pole of the Sun out to 1.5 AU (further at the edges) from STELab (left) and Ooty (right) density reconstructions. Earth's orbit is shown as a thin black circle with the Earth, a small \oplus , indicated on each plot (to the right in each image). The expected r^{-2} density fall-off scaling is used to normalize structures at different radii. Density contours to the left of each image are scaled to 1 AU.

reconstructions alone; not incorporating the IPS speeds at this time (as seen in Figs. 11 and 12). At this preliminary stage, even though the Ooty observations are more numerous than those of STELab, the resolution of the reconstructions was not increased. Two figures, both from 2004/11/08 at 00:00 UT show some similarities and differences between the density reconstructions from each IPS data set.

Figure 11 shows a side-by-side comparison cut in the ecliptic-plane as if looking down from the North pole of the Sun out to 1.5 AU (further at the edges). Figure 12 also shows a side-by-side comparison, this time a cut in the meridional-plane as if looking from 90° East of the Sun–Earth line out to a distance of 1.5 AU from the Sun (again further at the edges). In both figures, the STELab IPS density reconstruction-cut is on the left and the Ooty density reconstruction-cut is on the right. We are unsure if the anti-Earthward directed material reconstructed here only from the Ooty data is real or some kind of artefact from noise in the data propagating through into the reconstruction. The general structure seen to the North and East of the Sun–Earth line is seen in both reconstructions, but to a lesser extent to the East in the Ooty reconstruction. These are just preliminary comparisons at present, and a more-detailed analysis is expected to be undertaken in a forthcoming paper.

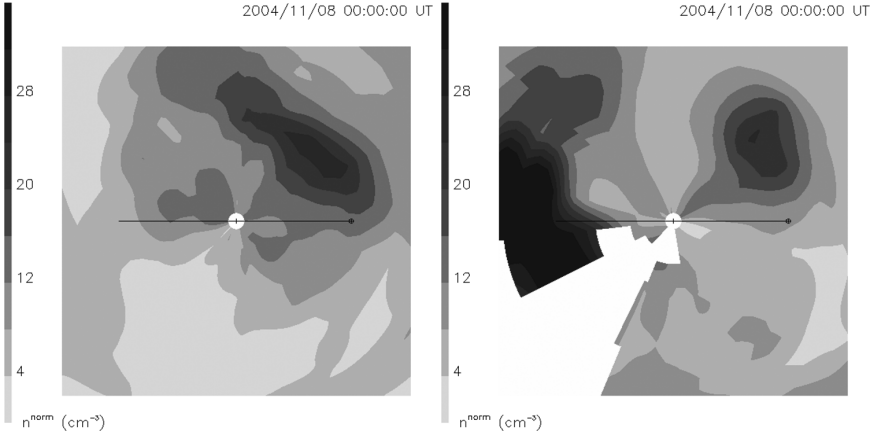


Fig. 12. Figure showing a side-by-side comparison cut in the meridional-plane as if looking from 90° East of the Sun–Earth line out to a distance of 1.5 AU from the Sun (further at the edges) from STELab (left) and Ooty (right) density reconstructions. Earth’s orbit is shown as a thin black line with the Earth, a small \oplus , indicated on each plot (to the right in each image). The expected r^{-2} density fall-off scaling is used to normalize structures at different radii. Density contours to the left of each image are scaled to 1 AU.

6. Summary

This chapter provides a brief summary of the most recent highlights of the 3D tomography reconstruction technique using both the co-rotating and the time-dependent kinematic models, and their applications to various IPS data sets and their extension to employ SMEI data. These include comparisons at Mars, comparisons with near-Earth *in situ* measurements, and also the constraining higher resolution extremely long-baseline IPS observations.

We have summarized the results of the IPS 3D reconstruction techniques in a comparison with *in situ* solar-wind ram-pressure analyses at Mars from the Mars Global Surveyor. This study does not specifically address the forecast capability of this technique at various positions in the inner heliosphere as demonstrated with our near-real-time analyses of the IPS data (http://ips.ucsd.edu/index_ss.html). However, these same modeling techniques provide a forecast of solar-wind conditions at Mars when the IPS arrays are operating, and also at other planets/spacecraft such as Mercury, Venus, Ulysses,⁴⁷ and both Solar TERrestrial Relations Observatory (STEREO)⁴⁸ spacecraft; thus they have the potential to

provide a forecast of solar-wind conditions almost anywhere in the inner heliosphere and sometimes several days in advance for points furthest from the Sun. No spacecraft at Mars currently monitors solar-wind velocity and density regularly. If *in situ* solar-wind monitoring instruments are present on spacecraft near the inner-planets for example, then comparisons with the IPS and/or SMEI 3D reconstructions should become even more relevant and the accuracy improved upon from the study discussed here.

Using the UCSD 3D density reconstructions from STELab IPS data to constrain the more-sensitive ELB observations from EISCAT and MERLIN has the potential to be a very powerful tool.^{31,32} It has resulted in our ability to retrieve further information than previously from these very few but highly sensitive observations to detect solar wind directionality and multiple streams along the line of sight. It is hoped that we will be able to use this technique to help constrain and better-fit ELB IPS observations in the future using both the STELab density reconstructions demonstrated here (and the constraining technique fully described in Ref. 31), and using the data from other IPS systems and, of course, from SMEI.

The geoeffective storms discussed here and by Refs. 29, 34, 42–44 are fairly well reproduced both in terms of the IPS speed 3D reconstructions and the preliminary SMEI density 3D reconstructions. They are consistent with the SOHO|LASCO events seen at that time and have been shown to be associated with known *in situ* signatures. The IPS data show the fast CME speeds seen in LASCO heading to the North and North-West as well as those engulfing Earth during the same time period. The structures reproduced around the Earth from SMEI data show a combination of several Earth-directed/near-Earth-directed events. These structures seen in SMEI are consistent with the timing of the geoeffective storms during this period.

The preliminary comparisons between the Ooty and the STELab data are a promising start. Already, without any additional calibration, similar features are seen in both reconstructed data sets. Overall, the Ooty data appear to show enhanced density values compared with the STELab density values when time-series of the two are compared, but we are working on improving this and if necessary, will perform a re-calibration of the kinematic solar wind model to work more accurately with the Ooty data and also aim for higher-resolutions by taking advantage of the more numerous IPS observations. Incorporating the Ooty speed data into the 3D

reconstructions will also aid in improving the accuracy of these preliminary reconstructions from data from the Ooty system.

In conclusion, we follow CMEs from near the solar surface outward until they are observed *in situ* near Earth and Mars, and at other points in the inner heliosphere and aim to compare in real-time with both STEREO spacecraft shortly, as is already being done routinely with ACE. These events, reconstructed in 3D in terms of both speed and density, show that the heliospheric response to CMEs is often enormous (from both various IPS data-sets and SMEI observations). We look forward to other (multi-point) *in situ* comparisons such as with Ulysses during its close-pass to the Sun recently in August 2007 and its quadrature earlier in 2007, and other such International Heliophysical Year (IHY) IPS collaborations. As our 3D tomographic models become more sophisticated, possibly incorporating a 3D MHD solar wind model, and multi-point calibrations are realized, we expect the comparisons to improve.

Acknowledgments

The authors acknowledge NSF grant FA8718-04-C-0050, NASA grant NNG05GM58G, and AFOSR grant FA9550-06-1-0107, to the University of California at San Diego (UCSD) for support to work on these analyses. The authors would especially like to thank the group at STELab, Nagoya University (M. Kojima, M. Tokumaru, K. Fujiki, and students) for their continued support, and for making IPS data sets available under the auspices of a joint collaborative agreement between the Center for Astrophysics and Space Sciences (CASS) at UCSD and STELab. Also wish to thank P. K. Manoharan for providing the Ooty (ORT) IPS g -level data and the Aberystwyth University IPS group (A. R. Breen and R. A. Fallows) for access to the EISCAT/MERLIN IPS data and results. SMEI was designed and constructed by a team of scientists and engineers from the US Air Force Research Laboratory, the University of California at San Diego, Boston College, Boston University, and the University of Birmingham in the UK. The authors wish to thank the ACE|SWEPAM group for use of the solar wind proton density and velocity measurements used in this chapter for *in situ* comparisons. In addition, the authors would like to thank both the LASCO and EIT consortia for the use of the SOHO|LASCO and SOHO|EIT images in this paper. Thanks also go to D. H. Crider for providing us with the Mars Global Surveyor *in situ* data for these analyses.

References

1. A. Hewish, P. F. Scott and D. Wills, *Nature* **203** (1964) 1214.
2. W. A. Coles and S. Maagoe, *Geophys. Res.* **77** (1972) 5622.
3. W. A. Coles, *Space Sci. Rev.* **72** (1995) 211.
4. R. A. Fallows, A. R. Breen, P. J. Moran, A. Canals and P. J. S. Williams, *Adv. Space Res.* **30** (2002) 437.
5. M. Kojima, A. R. Breen, K. Fujiki, K. Hayashi, T. Ohmi and M. Tokumaru, *J. Geophys. Res. (Space Phys.)* **109** (2004) 4103.
6. B. V. Jackson, J. A. Boyer, P. P. Hick, A. Buffington, M. M. Bisi and D. H. Crider, *Solar Phys.* **241** (2007) 385.
7. M. M. Bisi, R. A. Fallows, A. R. Breen, S. R. Habbal and R. A. Jones, *J. Geophys. Res. (Space Phys.)* **112** (2007) A06101.
8. P. P. Hick and B. V. Jackson, in *Proc. SPIE*, eds. S. Fineschi and M. A. Gummin (2004).
9. B. V. Jackson and P. P. Hick, *Astrophysics and Space Science, Lib. Vol. 314* (Kluwer Academic Publ., Dordrecht, 2005), pp. 355–386.
10. M. Kojima and T. Kakinuma, *J. Geophys. Res.* **92** (1987) 7269.
11. J. W. Armstrong and W. A. Coles, *J. Geophys. Res.* **77** (1972) 4602.
12. A. R. Breen, R. A. Fallows, M. M. Bisi, P. Thomasson, C. A. Jordan, G. Wannberg and R. A. Jones, *J. Geophys. Res. (Space Phys.)* **111** (2006) 8104.
13. M. M. Bisi, A. R. Breen, R. A. Fallows, G. D. Dorrian, R. A. Jones, G. Wannberg, P. Thomasson and C. Jordan, *EOS Trans. AGU, Fall Meeting Supp. — Abstract SH33A-0399* **87** (2006), p. 52.
14. W. A. Coles, *Astrophys. Space Sci.* **243**(1) (1996) 87.
15. M. Klinglesmith, PhD thesis, University of California, San Diego (UCSD) (1997).
16. M. M. Bisi, A. R. Breen, S. R. Habbal and R. A. Fallows, “Auld Reekie” *MIST/UKSP Joint Meeting*, Edinburgh, Scotland (2004) (Oral presentation).
17. G. Swarup, N. V. G. Sarma, M. N. Joshi, V. K. Kapahi, D. S. Bagri, S. H. Damle, S. Ananthkrishnan, V. Balasubramanian, S. S. Bhave and R. P. Sinha, *Nature* **230** (1971) 185.
18. P. K. Manoharan, M. Kojima, N. Gopalswamy, T. Kondo and Z. Smith, *Astrophys. J.* **530** (2000) 1061.
19. P. K. Manoharan, M. Tokumaru, M. Pick, P. Subramanian, F. M. Ipavich, K. Schenk, M. L. Kaiser, R. P. Lepping and A. Vourlidas, *Astrophys. J.* **559** (2001) 1180.
20. B. V. Jackson, P. P. Hick, M. Kojima and A. Yokobe, *J. Geophys. Res.* **103** (1998) 12049.
21. E. C. Stone, A. M. Frandsen, R. A. Mewaldt, E. R. Christian, D. Margolies, J. F. Ormes and F. Snow, *Space Sci. Rev.* **86** (1998) 1.
22. D. J. McComas, S. J. Bame, P. Barker, W. C. Feldman, J. L. Phillips, P. Riley and J. W. Griffee, *Space Sci. Rev.* **86** (1998) 563.
23. D. H. Crider, D. Vignes, A. M. Krymskii, T. K. Breus, N. F. Ness, D. L. Mitchell, J. A. Slavin and M. H. Acuña, *J. Geophys. Res. (Space Phys.)* **108** (2003) 1461.

24. P. H. Scherer, R. S. Bogart, R. I. Bush, J. T. Hoeksema, A. G. Kosovichev, J. Schou, W. Rosenberg, L. Springer, T. D. Tarbell, A. Title, C. J. Wolfson, I. Zayer and M. E. Team, *Solar Phys.* **162** (1995) 129.
25. G. E. Brueckner, R. A. Howard, M. J. Koomen, C. M. Korendyke, D. J. Michels, J. D. Moses, D. G. Socker, K. P. Dere, P. L. Lamy, A. Llebaria, M. V. Bout, R. Schwenn, G. M. Simnett, D. K. Bedford and C. J. Eyles, *Solar Phys.* **162** (1995) 357.
26. C. J. Eyles, G. M. Simnett, M. P. Cooke, B. V. Jackson, A. Buffington, P. P. Hick, N. R. Waltham, J. M. King, P. A. Anderson and P. E. Holladay, *Solar Phys.* **217** (2003) 319.
27. B. V. Jackson, A. Buffington, P. P. Hick, R. C. Altrock, S. Figueroa, P. E. Holladay, J. C. Johnston, S. W. Kahler, J. B. Mozer, S. Price, R. R. Radick, R. Sagalyn, D. Sinclair, G. M. Simnett, C. J. Eyles, M. P. Cooke, S. J. Tappin, T. Kuchar, D. Mizuno, D. F. Webb, P. A. Anderson, S. L. Keil, R. E. Gold and N. R. Waltham, *Solar Phys.* **225** (2004) 177.
28. M. M. Bisi, B. V. Jackson, P. P. Hick and A. Buffington, *LWS CDAW 2007 Meeting* (2007) (Oral presentation).
29. M. M. Bisi, B. V. Jackson, P. P. Hick and A. Buffington, *AOGS 2007 Meeting* (2007) (Oral presentation).
30. R. A. Jones, A. R. Breen, R. A. Fallows, M. M. Bisi, P. Thomasson, G. Wannberg and C. A. Jordan, *Annales Geophysicae* **24** (2006) 2413.
31. A. R. Breen, R. A. Fallows, M. M. Bisi, R. A. Jones, B. V. Jackson, M. Kojima, G. Dorrian, H. R. Middleton, P. Thomasson and G. Wannberg, *Astrophys. J. Lett.* **683** (2008) L79.
32. M. M. Bisi, B. V. Jackson, R. A. Fallows, A. R. Breen, P. P. Hick, G. Wannberg, P. Thomasson, C. A. Jordan and G. D. Dorrian, *Proceedings SPIE Optical Engineering + Applications 2007 Meeting*, April 2007.
33. J. P. Delaboudiniere, G. E. Artzner, J. Brunaud, A. Gabriel, J. F. Hochedez, F. Millier, X. Y. Song, B. Au, K. P. Dere, R. A. Howard, R. Kreplin, D. J. Michels, J. D. Moses, J. M. Defise, C. Jamar, P. Rochus, J. P. Chauvineau, J. P. Marioge, R. C. Catura, J. R. Lemen, L. Shing, R. A. Stern, J. B. Gurman, W. M. Eupert, A. Maucherat, F. Clette, P. Cugnon and E. L. van Dessel, *Solar Phys.* **162** (1995) 291.
34. M. M. Bisi, B. V. Jackson, P. P. Hick, A. Buffington, D. Odstrcil and J. M. Clover, *J. Geophys. Res. — Geomagnetic Storms of Solar Cycle 23* **113** (2008) A00A11, doi: 10.1029/2008JA01322.
35. P. Thomasson, *Quart. J. Royal Astron. Soc.* **27** (1986) 413.
36. H. Rishbeth and P. J. S. Williams, *Monthly Notices Royal Astron. Soc.* **26** (1985) 478.
37. G. Wannberg, L.-G. Vanhainen, A. Westman, A. R. Breen and P. J. S. Williams, in *Conference Proceedings, Union of Radio Scientists (URSI)* (2002).
38. P. J. Moran, A. R. Breen, C. A. Varley, P. J. S. Williams, W. P. Wilkinson and J. Markkanen, *Annales Geophysicae* **16** (1998) 1259.
39. M. M. Bisi, A. R. Breen, R. A. Fallows, P. Thomasson, R. A. Jones and G. Wannberg, in *ESA SP-592: Solar Wind 11/SOHO 16, Connecting Sun and Heliosphere*, September 2005.
40. M. M. Bisi, PhD thesis, The University of Wales, Aberystwyth (2006).

41. G. Wannberg, I. Wolf, L.-G. Vanhainen, K. Koskenniemi, J. Röttger, M. Postila, J. Markkanen, R. Jacobsen, A. Stenberg, R. Larsen, S. Eliassen, S. Heck and A. Huuskonen, *Radio Sci.* **32** (1997) 2283.
42. L. K. Harra, N. U. Crooker, C. H. Mandrini, L. van Driel-Gesztelyi, S. Dasso, J. Wang, H. Elliott, G. Attrill, B. V. Jackson and M. M. Bisi, *Solar Phys.* **244** (2007) 95, doi: 10.1007/s11207-007-9002-x.
43. J. Zhang, I. G. Richardson, D. F. Webb, N. Gopalswamy, E. Huttunen, J. C. Kasper, N. V. Nitta, W. Poomvises, B. J. Thompson, C.-C. Wu, S. Yashiro and A. N. Zhukov, *J. Geophys. Res.* **112** (2007) 10102.
44. J. Zhang, I. G. Richardson, D. F. Webb, N. Gopalswamy, E. Huttunen, J. C. Kasper, N. V. Nitta, W. Poomvises, B. J. Thompson, C.-C. Wu, S. Yashiro and A. N. Zhukov, *J. Geophys. Res.* **112** (2007) 12103.
45. B. V. Jackson, A. Buffington, P. P. Hick, X. Wang and D. Webb, *J. Geophys. Res. (Space Phys.)* **111** (2006) 4.
46. B. V. Jackson, M. M. Bisi, P. P. Hick, A. Buffington, J. M. Clover and W. Sun, *J. Geophys. Res. — Geomagnetic Storms of Solar Cycle 23* **113** (2008) A00A15, doi: 10.1029/2008JA013224.
47. F. P. Wenzel, R. G. Marsden, D. E. Page and E. J. Smith, *Astronomy and Astrophysics Supplement Series* **92** (1992) 207.
48. M. L. Kaiser, *Adv. Space Res.* **36** (2005) 1483.